Chemical Science

ROYAL SOCIETY OF CHEMISTRY

EDGE ARTICLE

View Article Online
View Journal

Cite this: DOI: 10.1039/d5sc03122b

All publication charges for this article have been paid for by the Royal Society of Chemistry

Facet engineering of MOF supports regulates product selectivity in CO_2 photoreduction by modulating electron and proton supply to COF shells

Hulin Shi,†[a] Zengrong Li,†[b] Shenglan Chen,[a] Yangtao Yao,[a] Linyi Wu,[a] Ruowen Shao,[a] Chang Sheng,[a] Shuxian Zhong,[b] Dongmei Wang,[a] Yuling Zhao,[a] Leihong Zhao[a] and Song Bai *[ab]

Selective photoreduction of CO_2 with H_2O to hydrocarbons is challenged by inadequate and uncontrollable electron and proton feeding. Herein, this limitation is overcome by integrating H_2O dissociation, CO_2 reduction, and O_2 evolution catalysts into a dual S-scheme heterojunction and regulating exposed facets of the heterojunction supports. In this design, H^+ and OH^- species generated by H_2O dissociation on the NH_2-MIL-125 support transfer to the T-COF shell and Fe_2O_3 insert for CO_2 reduction and O_2 evolution, respectively. Mechanistic investigations reveal that increasing NH_2-MIL-125{001} facet exposure promotes proton spillover, while simultaneously causing more active electrons to accumulate on the T-COF instead of NH_2-MIL-125. This suppresses H_2 evolution on the NH_2-MIL-125 core, directing more protons to the T-COF shell for CO_2 reduction. Consequently, the *CO intermediate becomes more prone to hydrogenation to CH_4 rather than desorption to CO or C–C coupling to form C_2 products, thereby progressively increasing CH_4 production while decreasing H_2, CO, C_2H_4, and C_2H_6 evolution. The three-in-one heterojunction with the highest proportion of NH_2-MIL-125{001} facets achieves a remarkable CH_4 productivity of 154.3 μmol g_{cat}^{-1} h^{-1} with a selectivity of 87.4%. This work highlights the synergistic advantages of heterojunction construction and facet engineering in concurrently optimizing electron and proton supply for CO_2 hydrogenation.

Received 29th April 2025
Accepted 26th August 2025

DOI: 10.1039/d5sc03122b

rsc.li/chemical-science

Introduction

Solar-driven conversion of carbon dioxide (CO_2) and water (H_2O) into value-added carbonaceous fuels and chemicals has garnered extensive attention from both industry and academia for mitigating global warming and addressing the energy crisis.[1,2] Generally, a variety of reduction products can be obtained due to the complex reaction steps and diverse intermediates involved. Among them, hydrocarbons such as methane (CH_4) are particularly desirable due to their higher energy densities and greater economic value.[3,4] However, achieving high activity and selectivity in photocatalytic upcycling of CO_2 to hydrocarbons remains challenging. The main reason is that the supply of hydrogen protons and the utilization efficiency of photogenerated carriers in most individual semiconductor photocatalysts are insufficient to sustain the multi-step proton-coupled electron transfer (PCET) processes.[5,6] As a result of the sluggish kinetics of PCET steps, CO_2-to-CO conversion, which involves fewer electrons and protons, is usually the dominant reaction in CO_2 valorization.[7,8] Furthermore, even when a semiconductor photocatalyst simultaneously possesses efficient charge separation efficiency and strong H_2O activation capability to provide ample electrons and protons, the absence of robust CO_2 adsorption and activation sites leads to preferential proton reduction over CO_2 hydrogenation. This results in H_2 emerging as the primary reduction product.[9]

To circumvent these challenges, it is highly desirable to develop novel photosynthetic systems that integrate components with complementary functionalities. In conventional hybrid catalyst designs, one component facilitates the feeding of protons by boosting water dissociation ($H_2O \rightarrow H^+ + OH^-$), but lacks the capacity to generate active electrons for reducing protons to H_2.[10–12] These protons then diffuse to a second component, which is rich in photoelectrons and effective in CO_2 reduction, giving rise to an acceleration of the PCET processes. While such tandem catalyst designs have demonstrated progress in CO_2 hydrogenation reactions, their practical

[a]Key Laboratory of the Ministry of Education for Advanced Catalysis Materials, College of Chemistry and Materials Science, Zhejiang Normal University, Jinhua, Zhejiang 321004, P. R. China. E-mail: songbai@zjnu.edu.cn

[b]Zhejiang Key Laboratory of Digital Intelligence Monitoring and Restoration of Watershed Environment, College of Geography and Environmental Sciences, Jinhua Normal University, Jinhua, Zhejiang 321004, P. R. China

† These authors contributed equally to this work.

implementation faces significant limitations. The uncontrollable supply of electrons and protons makes it difficult to regulate product selectivity, as the upgrading of CO_2 to different hydrocarbons requires varying numbers of electrons and protons.[13] Moreover, sluggish O_2 evolution kinetics substantially impair the efficiency of tandem CO_2 hydrogenation processes.[14] The marked disparity between CO_2 reduction and H_2O oxidation rates not only causes an accumulation of holes, exacerbating charge recombination, but also leads to an agglomeration of OH^-, impeding further H_2O decomposition. As a result, the supply of electrons and protons is reduced, which in turn constrains the progression of CO_2 hydrogenation reactions. To conquer these issues, the incorporation of auxiliary components that facilitate OH^- oxidation becomes essential. Specifically, integrating H_2O dissociation, CO_2 reduction, and O_2 evolution components into a three-in-one artificial photosynthetic system enables more balanced electron/hole and H^+/OH^- consumption, demonstrating significant potential for elevating the net efficiency of photoredox catalysis. Furthermore, strategic modulation of electron and proton distribution between the H_2O dissociation and CO_2 reduction components offers promising opportunities to fine-tune the product selectivity of these three-component photosynthetic systems.

Meticulous design and fabrication of heterojunction photocatalysts are crucial for optimizing synergistic effects between components.[15] Among various heterojunction types, S-scheme heterojunctions, which integrate both reduction and oxidation catalysts, have demonstrated superior photoinduced carrier separation ability while maintaining enhanced redox capabilities.[16,17] Recent studies have revealed that advancing from single to dual S-scheme heterojunctions confers two significant benefits: the generation of additional internal electric fields (IEFs) between components, enabling more efficient charge transfer and separation, and the creation of extra spatially separated redox sites that facilitate tandem reaction processes.[18,19] The spatial configuration of heterojunction photocatalysts is also of great importance. Core–shell architectures, featuring intimate interfacial contact and extensive contact area between components, offer distinct advantages by ensuring effective IEF formation and enhanced interfacial charge transfer.[20,21] The optimal arrangement positions the H_2O dissociation component at the core, encapsulated by a CO_2 reduction shell component. This configuration enables efficient outward diffusion of protons generated in the core, which then participate in CO_2 hydrogenation reactions at the shell surface.[22] A reversed arrangement would be suboptimal, as protons generated in the shell would diffuse away from the catalyst instead of toward the core sites, reducing their utilization efficiency. This optimal core–shell architecture also necessitates a porous shell structure to facilitate H_2O transport to the core and encourage proton migration to the shell.

Crystal facets exposed on the supports of core–shell structured S-scheme heterojunctions exert significant influence over both charge kinetics and surface reactivity.[23,24] Different facets exhibit diverse surface atomic arrangements and coordination environments, which give rise to varied surface energy band structures and distinct reactant adsorption/activation patterns. Such variations impact the IEF intensity, thereby affecting carrier separation efficiency, while also influencing H_2O dissociation rates and consequently the supply of active hydrogen.[25,26] Based on these mechanisms, facet engineering of supports in purposefully designed dual S-scheme heterojunction photocatalysts presents a promising strategy for controlling both electron and proton delivery during CO_2 hydrogenation, ultimately enabling precise regulation of product distribution. With the above thoughts in mind, in this work, NH_2-MIL-125(Ti) (MIL = Materials of Institute Lavoisier), a representative visible light-responsive metal–organic framework (MOF), with varying ratios of exposed {001} and {111} facets, was adopted to support Fe_2O_3 nanocrystals, affording well-defined S-scheme NH_2-MIL-125/Fe_2O_3 (NM/F) heterojunctions. These heterojunctions were further coated with T-COF (TAPT-BTCA-COF, TAPT = 2,4,6-tris(4-aminophenyl)-1,3,5-triazine, BTCA = 1,3,5-benzenetricarboxaldehyde) shells—a visible light-harvesting covalent organic framework (COF)—to create dual S-scheme NH_2-MIL-125/Fe_2O_3@T-COF (NM/F@T) heterojunctions. Combined experimental and theoretical results reveal that the NH_2-MIL-125 support is primarily responsible for splitting H_2O molecules into H^+ and OH^-, the Fe_2O_3 insert is committed to the oxidation of OH^- to O_2, and the T-COF shell accepts H^+ from the NH_2-MIL-125 core while catalyzing CO_2 reduction. Compared to the {111} facets of NH_2-MIL-125, NH_2-MIL-125{001} facets are more conducive to the adsorption and activation of H_2O molecules, resulting in enhanced H^+ generation. Additionally, increased exposure of {001} facets weakens the IEF between NH_2-MIL-125 and Fe_2O_3 but strengthens the IEF between Fe_2O_3 and T-COF, resulting in a higher distribution of photoelectrons in T-COF rather than NH_2-MIL-125. Consequently, fewer active electrons are available on the NH_2-MIL-125 core for H^+ consumption in H_2 production, promoting H^+ transfer to the T-COF shell for CO_2 reduction. The increased availability of electrons and protons favors the stepwise hydrogenation and deoxygenation of *CO intermediates over their desorption to CO or dimerization to *OCCO. As a result, the CH_4 yield of NM/F@T increases progressively as the percentage of {001} facets rises, while H_2, CO, C_2H_4, and C_2H_6 outputs follow the opposite trend. NM/F@T with maximum NH_2-MIL-125{001} facet exposure demonstrates excellent activity (154.3 μmol g_{cat}^{-1} h^{-1}) and selectivity (87.4%) in CO_2 methanation. To our knowledge, this is the first work that integrates H_2O dissociation, CO_2 reduction, and O_2 evolution catalysts into dual S-scheme heterojunctions for tandem CO_2 photofixation and regulates the product selectivity through MOF facet engineering.

Results and discussion

Catalyst synthesis and characterization

The synthetic routes for the NM/F and NM/F@T samples are illustrated schematically in Fig. 1a. First, NH_2-MIL-125 with varying percentages of {001} and {111} facets was prepared through a solvothermal process involving the reaction of titanium isopropoxide with 2-amino-1,4-benzenedicarboxylic acid

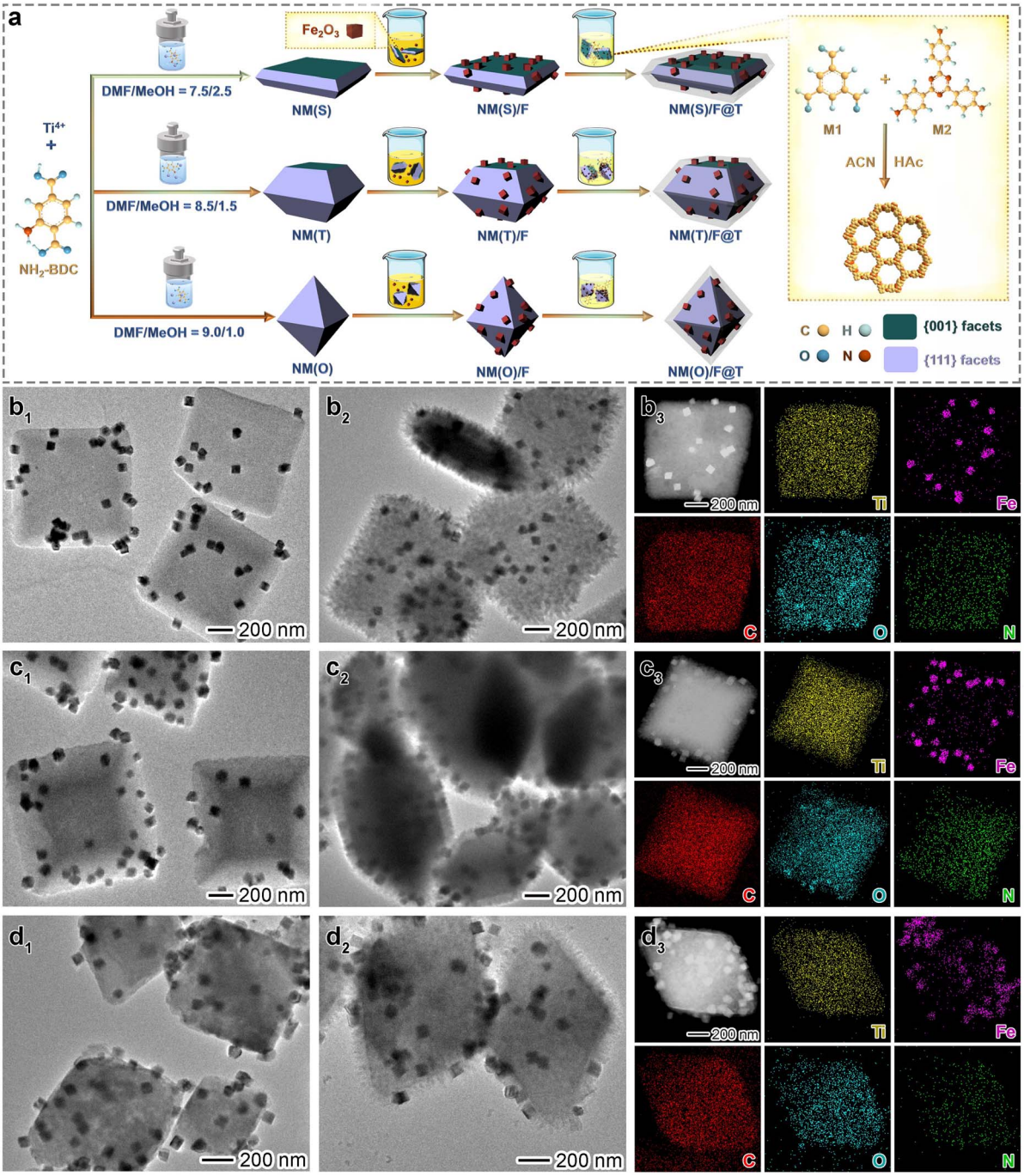

Fig. 1 Synthesis and electron microscopy characterization studies of NM/F and NM/F@T: (a) schematic illustration of the synthesis of NM/F and NM/F@T samples; (b_1–d_1) TEM images of (b_1) NM(S)/F, (c_1) NM(T)/F, and (d_1) NM(O)/F; (b_2–d_2) TEM, (b_3–d_3) STEM and EDS mapping images of (b_2 and b_3) NM(S)/F@T, (c_2 and c_3) NM(T)/F@T, and (d_2 and d_3) NM(O)/F@T.

(NH_2-BDC) in a mixture of *N*,*N*-dimethylformamide (DMF) and methanol (MeOH).[27] As the DMF/MeOH volume ratio increases from 7.5 : 2.5 to 8.5 : 1.5, and then to 9.0 : 1.0, the NH_2-MIL-125 nanocrystals exhibit distinct morphologies: sheet, truncated octahedron, and octahedron, which are denoted as NM(S), NM(T), and NM(O), respectively. As revealed by scanning electron microscopy (SEM) (Fig. S1), the morphological evolution of NH_2-MIL-125 from a sheet to a truncated octahedron, and eventually to an octahedron, is characterized by a gradual shrinkage of the top and bottom {001} facets, accompanied by a stepwise expansion of the eight side {111} facets. As a result, the average percentage of exposed {111} facets increases from 43% to 78%, and then to 100% for NM(S), NM(T), and NM(O), respectively (Fig. S2 and Table S1). Subsequently, Fe_2O_3 nanocubes with an average edge length of around 65 nm and exposed crystal planes of (012)/(10$\bar{2}$) were pre-synthesized (Fig. S3),[28] and

then deposited onto the surfaces of NM(S), NM(T), and NM(O) to create NM(S)/F, NM(T)/F, and NM(O)/F, respectively. Transmission electron microscopy (TEM) and SEM images (Fig. 1b$_1$, c$_1$, d$_1$ and S4a$_1$, b$_1$, c$_1$) show that cubic Fe_2O_3 nanocrystals are evenly distributed on the surface of NH_2-MIL-125, establishing seamless face-to-face contact. Finally, by condensing benzene-1,3,5-tricarbaldehyde (M1) and 2,4,6-tris(4-aminophenyl)-1,3,5-triazine (M2) in a mixture of acetonitrile (ACN) and acetic acid (HAc),[29] NM(S)/F, NM(T)/F, and NM(O)/F were coated with T-COF to produce NM(S)/F@T, NM(T)/F@T, and NM(O)/F@T, respectively. TEM and SEM observations reveal that needle-like T-COF uniformly covers the NH_2-MIL-125 surface (Fig. 1b$_2$, c$_2$, d$_2$, and S4a$_2$, b$_2$, c$_2$). No protrusion of the T-COF shell is observed on the top of Fe_2O_3, suggesting that both T-COF and Fe_2O_3 supported by NH_2-MIL-125 are exposed to the atmosphere, with lateral contact between them. This arrangement creates well-defined MOF@COF core–shell heterostructures, featuring Fe_2O_3 partially embedded within the COF shell and the coexistence of MOF-Fe_2O_3, Fe_2O_3-COF, and MOF-COF heterointerfaces. In the high-resolution TEM (HRTEM) images of NM/F@T samples, the lattice fringes at the triple-phase interfaces of NH_2-MIL-125, Fe_2O_3, and T-COF are obscured because both the MOF core and COF shell lose crystallinity upon exposure to electron beam irradiation, owing to the susceptibility of light elements in the organic portions to high-energy electrons (Fig. S5). Scanning TEM (STEM) images of NM/F@T samples, along with their corresponding elemental mapping, further substantiate that the Ti-rich NH_2-MIL-125 cores are decorated with Fe_2O_3 inserts and simultaneously enveloped by homogeneous N-rich T-COF shells (Fig. 1b$_3$, c$_3$, and d$_3$).

NM(S), NM(T), and NM(O) exhibit similar powder X-ray diffraction (XRD) patterns that align with the simulated results, indicating their high purity and crystallinity (Fig. S6). The diffraction peaks of Fe_2O_3 correspond to the rhombohedral phase hematite (JCPDS 33-0664), while T-COF peaks match well with the simulated AA stacking mode.[30] Characteristic peaks of NH_2-MIL-125, Fe_2O_3, and T-COF appear simultaneously in the XRD patterns of NM/F@T samples, verifying the successful construction of three-phase heterojunctions. The optical properties of the samples were analyzed using UV-vis diffuse reflectance spectroscopy (DRS). NM(S), NM(T), NM(O), Fe_2O_3, and T-COF exhibit strong absorption in the visible region, with corresponding bandgaps (E_g) determined to be 2.66, 2.63, 2.65, 1.83, and 2.71 eV, respectively (Fig. S7 and S8). NM/F@T samples display similar UV-vis DRS profiles that reflect a simple superposition of the spectra of their constituent components, indicating that photon absorption does not significantly impact their ultimate photocatalytic performance. N_2 sorption experiments reveal that the Brunauer–Emmett–Teller (BET) specific surface areas of NH_2-MIL-125 samples range from 733.2 to 815.5 $m^2\ g^{-1}$, exceeding those of Fe_2O_3 (9.8 $m^2\ g^{-1}$) and T-COF (606.8 $m^2\ g^{-1}$) (Fig. S9 and Table S2). NM(S)/F@T, NM(T)/F@T, and NM(O)/F@T exhibit comparable BET areas, ranging from 347.4 to 391.3 $m^2\ g^{-1}$, which eliminates the influence of surface area differences on their photocatalytic properties. The reduced surface areas of NM/F@T samples compared to NH_2-MIL-125 and T-COF are likely attributed to the mass occupation by Fe_2O_3. Inductively coupled plasma-mass spectroscopy (ICP-MS) results indicate approximate contents of NH_2-MIL-125 and Fe_2O_3 in different NM/F and NM/F@T samples, ruling out any compositional effects on their photocatalytic activities (Table S3).

Photocatalytic performance analysis

Armed with the structural and compositional information of NH_2-MIL-125, NM/F, and NM/F@T, we evaluated their photocatalytic CO_2 reduction performance in a solid–gas reactor (Fig. S10), using water vapor as the proton donor without any sacrificial agents. As shown in Fig. 2a–c, all NH_2-MIL-125 samples primarily produce H_2, accompanied by small amounts of CO and CH_4 as CO_2 reduction products. The H_2 evolution rates and selectivities decrease in the order: NM(S) > NM(T) > NM(O), while CO and CH_4 activities and selectivities follow the reverse sequence. This pattern suggests that the {001} facets of NH_2-MIL-125 are more favorable for H_2 generation but less active in reducing CO_2 compared to the {111} facets, consistent with previous reports.[31,32] When NH_2-MIL-125 combines with Fe_2O_3, there is a significant elevation of H_2, CO, and CH_4 outputs. Notably, the photocatalytic enhancement becomes more pronounced as the proportion of NH_2-MIL-125{111} facets increases. Consequently, the yields of H_2, CO, and CH_4 escalate in the following order: NM(S)/F < NM(T)/F < NM(O)/F. The subsequent T-COF coating further augments CO and CH_4 evolution rates of NM/F@T while suppressing H_2 production, thereby improving selectivity toward CO and CH_4 formation. This behavior underscores the pivotal role of T-COF in promoting CO_2 reduction while inhibiting the competing proton reduction pathway. In addition to H_2, CO, and CH_4, the NM/F@T samples also produce trace quantities of C_2H_4 and C_2H_6, indicating that the presence of T-COF also enhances the transformation of CO_2 to C_2 products (Fig. 2d and e). Notably, both the productivity and selectivity of NM/F@T for H_2, CO, C_2H_4, and C_2H_6 evolution display a progressive augmentation in the sequence NM(S)/F@T < NM(T)/F@T < NM(O)/F@T. CH_4, however, is an exception, with its productivity and selectivity following the opposite trend. As such, NM(S)/F@T delivers the highest CH_4 evolution rate of 154.3 μmol $g_{cat}^{-1}\ h^{-1}$, along with the maximum CH_4 selectivity of 87.4% among the samples. These values are 1.8/1.5 and 3.6/3.3 times higher than those of NM(T)/F@T and NM(O)/F@T, respectively. Moreover, NM(S)/F@T demonstrates the most dramatic improvements in CO_2 methanation after T-COF incorporation, furnishing a 120.5-fold increase in CH_4 activity and a 57.6-fold enhancement in CH_4 selectivity compared to NM(S)/F. In contrast, NM(T)/F@T and NM(O)/F@T exhibit more moderate gains, with CH_4 activity and selectivity increasing by factors of 25.8/20.4 and 6.0/4.8, respectively, relative to their binary counterparts. These results collectively corroborate a strong correlation between the photocatalytic performance of the samples and the exposed facet of NH_2-MIL-125.

Regarding the H_2O oxidation half reaction, O_2 was the sole detected product. Fig. 2f clearly reveals a progressive decline in the O_2 release rate of NH_2-MIL-125 as its morphology

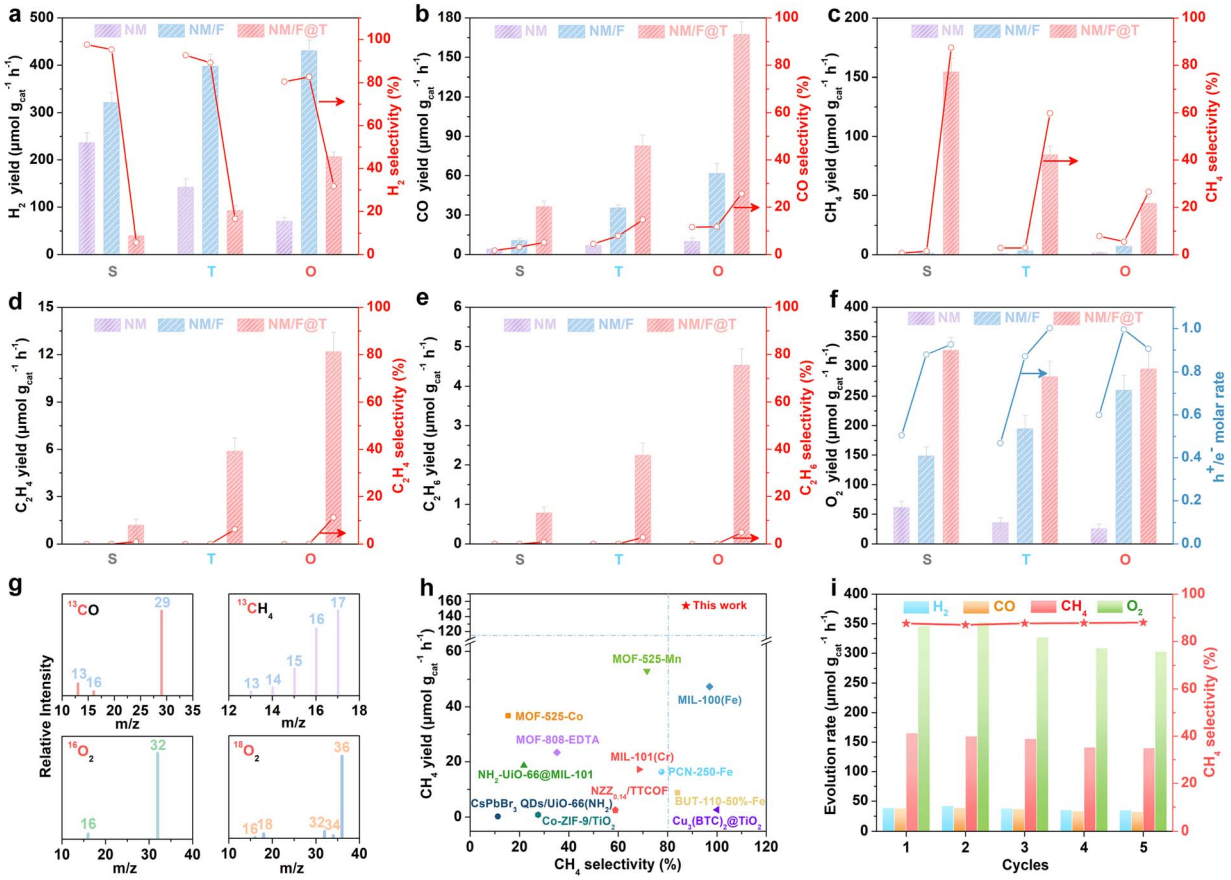

Fig. 2 Photocatalytic performance of NH_2-MIL-125, NM/F, and NM/F@T: (a–e) product yields and selectivities for (a) H_2, (b) CO, (c) CH_4, (d) C_2H_4, and (e) C_2H_6; (f) O_2 yields and hole/electron utilization ratios; (g) mass spectra of ^{13}CO, $^{13}CH_4$, $^{16}O_2$, and $^{18}O_2$ produced from $^{13}CO_2$ and $H_2{}^{18}O$ isotope experiments over NM(S)/F@T; (h) comparison of CH_4 productivity and selectivity of NM(S)/F@T with existing MOF- and COF-based catalysts; (i) recycling tests over NM(S)/F@T (the yields of C_2 products are too low to be displayed in Fig. 2i).

transitions from sheets to truncated octahedra, and finally to octahedra, mirroring the trend observed in their H_2 outputs. For all NH_2-MIL-125 variants, O_2 productivity increases incrementally with sequential Fe_2O_3 deposition and T-COF coating. Notably, the magnitude of this enhancement greatly depends on the shape of NH_2-MIL-125. In the case of NM(S), the Fe_2O_3 deposition and COF coating lead to 2.4-fold and 2.2-fold increases in O_2 yield, respectively. As for NM(T) and NM(O), these values are 5.4/1.5 and 10.0/1.1, respectively. That is to say, the O_2 evolution enhancement induced by Fe_2O_3 anchoring becomes more significant with a larger proportion of NH_2-MIL-125{111} facets, while the enhancement from the T-COF coating is more pronounced when there is a greater percentage of NH_2-MIL-125{001} facets. Based on the evolution rates of redox products and the number of photocarriers required for their generation ($H^+ + 2e^- \rightarrow H_2$; $CO_2 + 2H^+ + 2e^- \rightarrow CO + H_2O$; $CO_2 + 8H^+ + 8e^- \rightarrow CH_4 + 2H_2O$; $2CO_2 + 12e^- + 12H^+ \rightarrow C_2H_4 + 4H_2O$; $2CO_2 + 14e^- + 14H^+ \rightarrow C_2H_6 + 4H_2O$; $2H_2O + 4h^+ \rightarrow O_2 + 4H^+$), the molar ratios between hole and electron utilization rates were calculated. As shown in Fig. 2f, for all NH_2-MIL-125 samples, this ratio falls far below the theoretical value of 1, inferring that H_2O oxidation lags behind CO_2 reduction. In contrast, the ratios for NM/F samples range from 0.87 to 1.00, and the range does not change significantly upon the subsequent addition of T-COF. This suggests that Fe_2O_3 plays a crucial role in facilitating O_2 generation, effectively optimizing the balance between CO_2 reduction and H_2O oxidation.

Control experiments without a catalyst or light irradiation were conducted. Under these circumstances, no H_2, O_2, or carbonaceous products were detected, confirming the photocatalytic nature of the CO_2 reduction and H_2O oxidation reactions (Fig. S11). To further identify the carbon source of the main carbon-containing products, ^{13}C isotopic labeling experiments were carried out. As displayed in Fig. 2g, mass spectrometry (MS) signals with m/z values of 29 and 17 can be assigned to ^{13}CO and $^{13}CH_4$, respectively, providing unambiguous evidence that the C_1 products are derived from CO_2 reduction.[33] Additionally, when $H_2{}^{16}O$ is replaced by $H_2{}^{18}O$ as the reactant, a new MS signal at $m/z = 36$ emerges, attributable to $^{18}O_2$, validating that the produced O_2 stems from H_2O oxidation.[34] The photocatalytic performance of NM(S)/F@T in CO_2 methanation surpasses that of most existing MOF and COF-based catalysts in terms of both activity and selectivity (Fig. 2h and Table S4). The apparent quantum efficiency (AQE) for CH_4 evolution, when plotted as a function of absorption wavelength, closely correlates with the UV-vis DRS of NM(S)/

F@T, peaking at 3.32% under 400 nm irradiation (Fig. S12). The photoactivity of NM(S)/F@T was also rigorously evaluated under various concentrations of diluted CO_2 atmospheres. The CH_4 activity and selectivity remain relatively stable when the CO_2/(Ar + CO_2) volume ratio varies from 50% to 100% (Fig. S13). Even when using a 15%CO_2/85%Ar mixture as the gas source, NM(S)/F@T affords a CH_4 yield of 64.6 μmol g_{cat}^{-1} h^{-1} and a selectivity of 68.0%, approximately 41.9% and 77.8% of those measured in pure CO_2, respectively. This excellent photocatalytic performance under a diluted CO_2 atmosphere can be ascribed to the synergy of the porous MOF core and COF shell in enhancing CO_2 capture and enrichment. To assess the durability of NM(S)/F@T, five consecutive photocatalytic cycles were performed, each lasting 4 h. As shown in Fig. 2i, by the fifth cycle, all the product yields from CO_2 reduction and H_2O oxidation remain above 83.9% of the initial cycle, without obvious fading in CH_4 selectivity. The excellent stability and reusability of the NM(S)/F@T catalyst can be ascribed to its stable structure and composition, as verified by comparative XRD, TEM, and X-ray photoelectron spectroscopy (XPS) analyses before and after cycling tests (Fig. S14–S16). Similarly, the used NM(T)/F@T and NM(O)/F@T catalysts also exhibit structures and morphologies similar to their fresh counterparts, suggesting that the stability of NM/F@T is unrelated to the exposed crystal facets of the NH_2-MIL-125 substrate (Fig. S17 and S18).

Facet-dependent photocatalytic mechanisms of NH_2-MIL-125

To gain a comprehensive understanding of the facet-dependent photocatalytic performance of NH_2-MIL-125, the separation efficiency of photogenerated carriers was judged by photoluminescence (PL) spectra. As shown in Fig. S19, the PL intensity of NM(T) is lower than that of NM(O) but higher than that of NM(S), indicating a progressive reduction in radiative charge recombination with increased exposure of the {001} facets. Complementary photoelectrochemical (PEC) measurements further substantiate this trend. Specifically, NM(S) exhibits the highest photocurrent density and the smallest electrochemical impedance spectroscopy (EIS) arc radius, followed by NM(T) and NM(O), suggesting decreasing charge separation efficiency and increasing carrier transfer resistance (R_{ct}) (Fig. S20, S21 and Table S5). The origins of this phenomenon were systematically investigated by comparing the local coordination environments of the {001} and {111} facets. As illustrated in Fig. 3a and b, the NH_2-MIL-125{001} facets predominantly comprise saturated six-coordinated Ti atoms (Ti_{6c}), whereas the NH_2-MIL-125{111} facets contain both Ti_{6c} and low-coordinated Ti atoms (Ti_{4c} and Ti_{5c}). Previous research has demonstrated that saturated Ti_{6c} atoms are more efficient at accepting photoelectrons from ligands *via* the reduction of Ti^{4+} to Ti^{3+}, in comparison to their less-coordinated Ti_{4c} and Ti_{5c} counterparts.[31] To rigorously validate this point, electron paramagnetic resonance (EPR) measurements were conducted under both dark and light irradiation conditions. As presented in Fig. 3c, NM(S), NM(T), and NM(O) samples exhibit weak EPR signals at $g = 1.947$ with comparable intensities in the dark, indicative of a small quantity of Ti^{3+} species. Upon light illumination, the EPR signals of all samples intensify, following distinct amplitudes: NM(S) > NM(T) > NM(O). This trend suggests that a greater proportion of

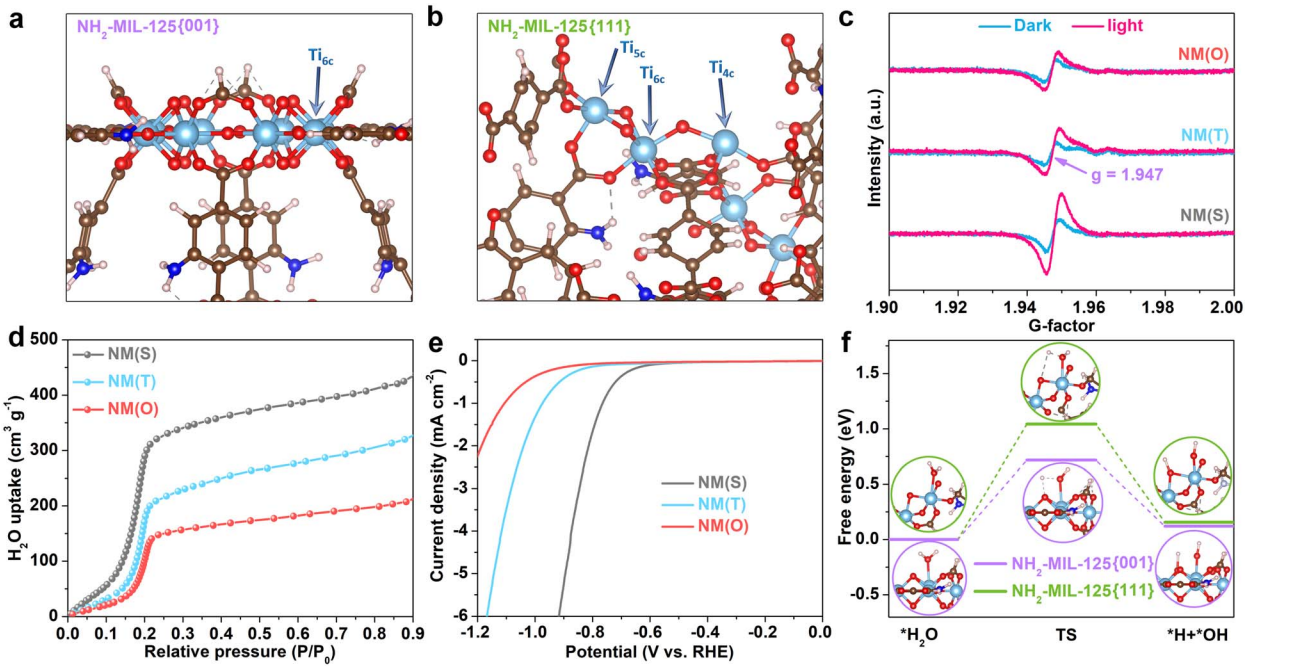

Fig. 3 Facet-dependent H_2O dissociation abilities of NH_2-MIL-125: (a and b) structure models of (a) NH_2-MIL-125{001} and (b) NH_2-MIL-125{111} facets (brown: C, blue: N, red: O, azure: Ti, white: H); (c) EPR spectra of NM(S), NM(T), and NM(O) under dark conditions and light irradiation; (d) water vapor adsorption isotherms of NM(S), NM(T), and NM(O); (e) LSV curves of NM(S), NM(T), and NM(O) for the HER; (f) Gibbs free energy of transition states for H_2O dissociation on NH_2-MIL-125{001} and NH_2-MIL-125{111} facets.

Ti^{4+} is reduced to Ti^{3+} as the percentage of {001} facets increases. The formation of Ti^{3+} is further corroborated by a color change from the original yellow to brown when NH_2-MIL-125 samples, dispersed in water, are irradiated with visible light under a N_2 atmosphere (Fig. S22). Obviously, the brown coloration deepens progressively with an increasing content of {001} facets, providing additional evidence for the involvement of more photoinduced electrons in the reduction of Ti^{4+}.[35,36] Therefore, it can be concluded that NH_2-MIL-125{001} facets, characterized by a higher concentration of Ti_{6c} atoms, demonstrate superior capability in capturing photoelectrons, thereby enhancing charge separation.

In addition to charge separation and transfer kinetics, the facet effect on the surface reaction kinetics of the NH_2-MIL-125 samples was also examined. As disclosed by water vapor adsorption isotherms in Fig. 3d, NM(S) presents the highest water vapor uptake, while NM(O) shows the lowest uptake among the three samples. This observation suggests that NH_2-MIL-125{001} facets are more favorable for the adsorption of H_2O molecules compared to NH_2-MIL-125{111} facets. The water contact angles on NM(S), NM(T), and NM(O) surfaces are 45.1°, 75.2°, and 82.5°, respectively, unveiling the higher hydrophilicity of NH_2-MIL-125{001} facets relative to NH_2-MIL-125{111} facets (Fig. S23). Linear sweep voltammetry (LSV) curves for the hydrogen evolution reaction (HER) reveal that the overpotential ranks in the order NM(S) < NM(T) < NM(O) (Fig. 3e). This trend reflects more efficient HER kinetics on the NH_2-MIL-125{001} facets relative to the {111} facets. To elucidate the underlying mechanism, we simulated the energy profiles of H_2O dissociation on the NH_2-MIL-125{001} and NH_2-MIL-125{111} facets using density functional theory (DFT) calculations. As shown in Fig. 3f, the dissociation of $*H_2O$ into *H and *OH on {111} requires overcoming an energy barrier of 1.04 eV. In contrast, {001} exhibits a lower energy barrier of 0.72 eV, indicating superior H_2O activation ability to cleave O–H bonds and consequently enhanced proton generation for H_2 generation.[37] Taken together, the combined effects of better H_2O adsorption and activation behaviors, coupled with the greater electron trapping capabilities of NH_2-MIL-125{001}, facilitate more efficient proton reduction, contributing to the superior photoactivity of NM(S) in H_2 evolution.

Facet-dependent charge kinetics of NM/F and NM/F@T

In order to comprehensively elucidate the mechanisms underlying the photocatalytic enhancements of NH_2-MIL-125 enabled by Fe_2O_3 loading and T-COF coating, transient photocurrent and electrochemical impedance spectroscopy (EIS) measurements were conducted on NM/F and NM/F@T samples, utilizing individual components as controls. As displayed in Fig. S24, all NM/F samples exhibit higher photocurrent responses than Fe_2O_3 and the corresponding NH_2-MIL-125, evincing the synergistic effect of the two components in reinforcing charge separation. Specifically, the photocurrent densities of NM(S)/F, NM(T)/F, and NM(O)/F are 1.41, 1.61, and 2.34 times higher than those of NM(S), NM(T), and NM(O), respectively (Fig. 4a). This outcome mirrors more efficient charge separation when Fe_2O_3 is combined with NH_2-MIL-125 {111} facets relative to NH_2-MIL-125{001} facets. EIS Nyquist plots further corroborate these findings, revealing a variable reduction in the R_{ct} of NH_2-MIL-125 after Fe_2O_3 deposition. The magnitude of this decline follows a distinct progression: NM(S)/F < NM(T)/F < NM(O)/F, providing additional evidence of the facet-dependent interfacial charge transfer dynamics (Fig. S25 and Table S5). Full encapsulation of NM/F samples within T-COF leads to further improvements in photocurrent responses, indicating enhanced charge separation efficiencies in NM/F@T samples (Fig. S24). In particular, NM(S)/F@T, NM(T)/F@T, and NM(O)/F@T exhibit 1.82-, 1.43-, and 1.26-fold increases in photocurrent densities compared to their respective NM/F counterparts (Fig. 4a). This result suggests that more pronounced carrier separation occurs when the NH_2-MIL-125{001} facets of NM/F are covered by T-COF. EIS results manifest that the extent of R_{ct} reduction in the ternary samples positively correlates with the observed photocurrent enhancements, providing compelling support for this finding (Fig. S25 and Table S5).

To unravel the facet-dependent charge separation efficiencies of NM/F and NM/F@T, we investigated the charge-transfer mechanisms between NH_2-MIL-125, Fe_2O_3, and T-COF by analyzing their energy band structures. Ultraviolet photoelectron spectroscopy (UPS) spectra (Fig. S26) reveal the work functions (W_F) of NM(S), NM(T), NM(O), Fe_2O_3, and T-COF as 4.70, 4.46, 4.25, 5.65, and 4.40 eV, respectively. Accordingly, their Fermi levels (E_F) are positioned at −4.70, −4.46, −4.25, −5.65, and −4.40 eV relative to the vacuum level (eV *vs.* vacuum). Based on the UPS valence-band spectra, the highest occupied molecular orbital (HOMO)/valence band maximum (VBM) of NM(S), NM(T), NM(O), Fe_2O_3, and T-COF is located at 2.05, 2.04, 2.13, 1.50, and 1.85 eV below the E_F. Consequently, their absolute positions were calculated to be −6.75, −6.50, −6.38, −7.15, and −6.25 eV, respectively. Considering their E_g, the corresponding lowest unoccupied molecular orbital (LUMO)/conduction band minimum (CBM) values were determined to be −4.09, −3.87, −3.73, −5.32, and −3.54 eV. Applying the numerical difference of 4.44 V to convert the absolute vacuum energy to the normal hydrogen electrode potential at pH = 0, the E_F, LUMO/CBM, and HOMO/VBM positions of NM(S), NM(T), NM(O), Fe_2O_3, and T-COF were established as 0.26/−0.35/2.31, 0.02/−0.57/2.06, −0.19/−0.71/1.94, 1.21/0.88/2.71, and −0.04/−0.90/1.81 V *vs.* NHE, respectively. As depicted in Fig. 4b, the E_F, LUMO, and HOMO of NH_2-MIL-125 progressively shift upward as the proportion of {111} facets increases from NM(S) to NM(T) and then to NM(O), in line with the previous report.[38] This trend is corroborated by theoretical simulations, which reveal that the W_F of NH_2-MIL-125{001} facets (5.09 eV) is markedly larger than that of NH_2-MIL-125 {111} (4.43 eV) (Fig. S27). Moreover, the E_F, CBM, and VBM of Fe_2O_3 are positioned at lower energy levels relative to the corresponding E_F, LUMO, and HOMO of NH_2-MIL-125 and T-COF. In view of their staggered band alignment, EPR experiments were employed to identify the charge transfer directions between them using 5,5-dimethyl-1-pyrroline *N*-oxide (DMPO) as a free radical trapping agent. As shown in Fig. S28, under

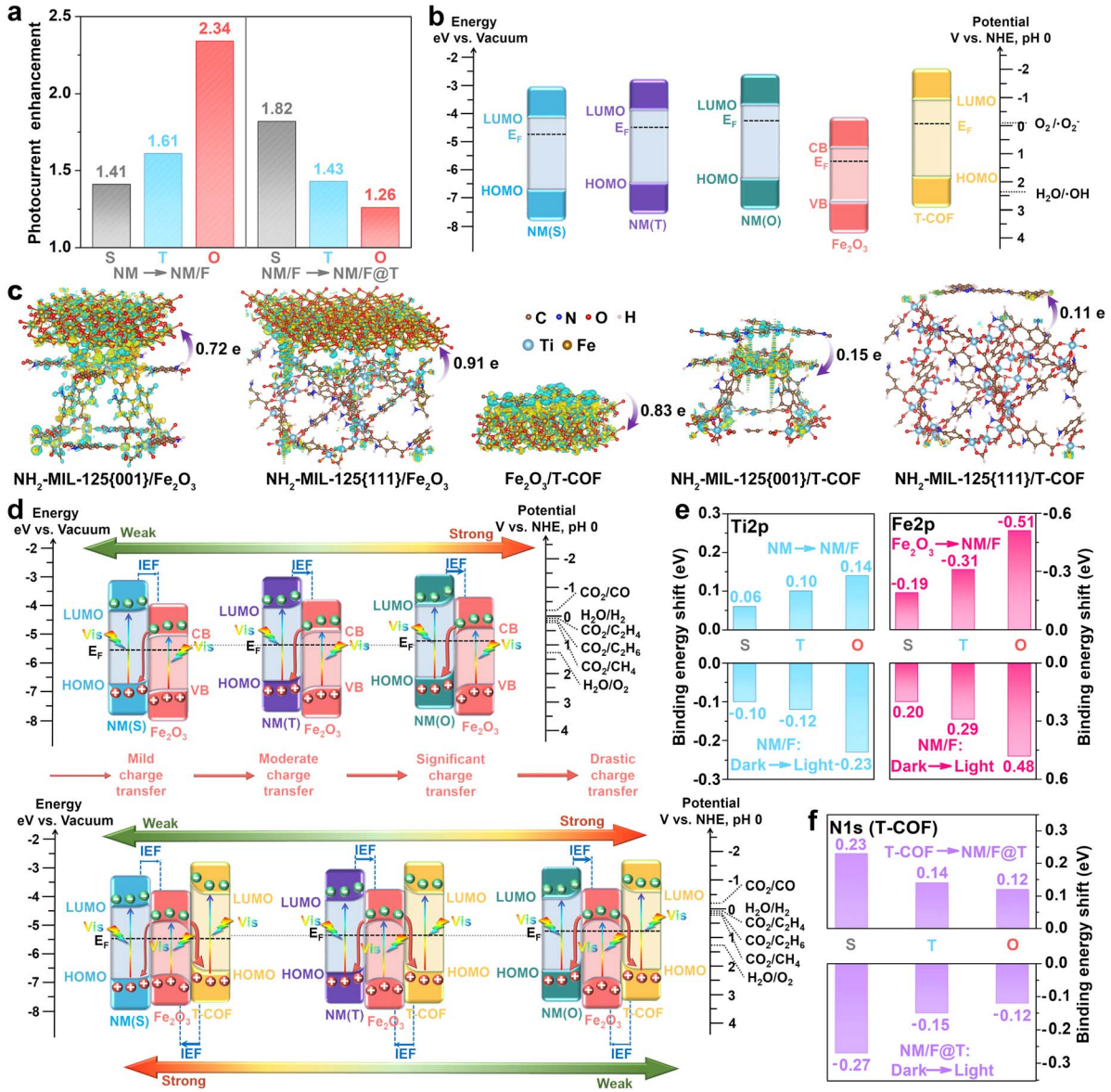

Fig. 4 Facet-dependent charge kinetics of NM/F and NM/F@T: (a) photocurrent enhancements of NH_2-MIL-125 after Fe_2O_3 loading and T-COF coating; (b) energy band structures of NM(S), NM(T), NM(O), Fe_2O_3, and T-COF; (c) charge density differences of NH_2-MIL-125{001}/Fe_2O_3, NH_2-MIL-125{111}/Fe_2O_3, Fe_2O_3/T-COF, NH_2-MIL-125{001}/T-COF, and NH_2-MIL-125{111}/T-COF heterointerfaces (electron accumulation and depletion are represented by the yellow and blue regions, respectively, the isosurface is 0.0015 electron per $Å^3$); (d) schematic illustrating the charge transfer in NM/F (top) and NM/F@T (bottom); (e) Ti 2p and Fe 2p binding energy shifts of NH_2-MIL-125 and Fe_2O_3 after their hybridization and then under light irradiation; (f) N 1s binding energy shifts of T-COF after its integration with NM/F and then under light irradiation.

light excitation, no DMPO–$\cdot O_2^-$ signal is detected for Fe_2O_3, because its CBM is less negative than the $O_2/\cdot O_2^-$ reduction potential. Similarly, NM(S) and T-COF show no DMPO–·OH signal, given that their HOMOs are less positive than the H_2O/·OH oxidation potential. Contrastingly, NM(S)/F produces both DMPO–$\cdot O_2^-$ and DMPO–·OH signals, with intensities higher than those of its individual components. This observation precludes the formation of a type-II heterojunction, as such a junction would prevent the generation of $\cdot O_2^-$ and ·OH radicals.[39] NM(S)/F@T also creates both DMPO–$\cdot O_2^-$ and DMPO–·OH adducts, but with notably higher intensities than NM(S)/F. These features further affirm the stepwise enhancement of charge separation efficiency as the number of components increases. Additionally, the charge density differences of NH_2-MIL-125{001}/Fe_2O_3, NH_2-MIL-125{111}/Fe_2O_3, Fe_2O_3/T-COF, NH_2-MIL-125{001}/T-COF, and NH_2-MIL-125{111}/T-COF heterointerfaces involved in the NM/F and NM/F@T samples were calculated and are shown in Fig. 4c. For the first three heterointerfaces, negative charges predominantly accumulate on the Fe_2O_3 side, while positive charges are mainly distributed on the NH_2-MIL-125 and T-COF sides, reflecting the flow of free electrons from NH_2-MIL-125 and T-COF to Fe_2O_3 upon contact. Bader charge analysis further reveals that the electron transfer amounts from NH_2-MIL-125{001}, NH_2-MIL-

125{111}, and T-COF to Fe_2O_3 are 0.72, 0.91, and 0.83 *e*, respectively, authenticating greater electron donation from NH_2-MIL-125{111} facets relative to NH_2-MIL-125{001} facets. For the latter two interfaces, charge redistributions are less pronounced, with significantly smaller Bader charges (0.15 and 0.11*e*) compared to the former three interfaces, indicating that no effective electric field can be established to drive the transport of photogenerated charge carriers. This difference is primarily attributed to the smaller E_F disparities between NH_2-MIL-125 and T-COF compared to their respective disparities with Fe_2O_3.

Building on the preceding discussion, an S-scheme charge transfer pathway is proposed for the NM/F samples. As illustrated in Fig. 4d, the E_F level of Fe_2O_3 is lower than that of NH_2-MIL-125 samples, causing free electrons to flow spontaneously from the latter to the former upon contact until E_F equilibrium is reached. This process gives rise to an IEF directed from NH_2-MIL-125 to Fe_2O_3, accompanied by upward band bending (BB) of NH_2-MIL-125 and downward BB of Fe_2O_3 around the interfaces. Upon photoexcitation of the two components, the IEF and BB induce the transfer of photoinduced electrons from the conduction band (CB) of Fe_2O_3 across the heterointerfaces, where they recombine with holes in the HOMO of NH_2-MIL-125. Concurrently, high-energy electrons in the NH_2-MIL-125 LUMO and holes in the Fe_2O_3 valence band (VB) remain available for potential redox reactions. Notably, as the percentage of NH_2-MIL-125{111} facets grows from NM(S) to NM(T) and then to NM(O), the E_F difference between NH_2-MIL-125 and Fe_2O_3 becomes more pronounced. This escalating discrepancy facilitates a more significant flow of free electrons upon hybridization of the two components. As a result, the IEF is amplified and the BB is intensified, accelerating the S-scheme transfer and recombination of low-energy charges. This, in turn, enables more efficient separation of active carriers for surface reactions. The aforementioned mechanism provides a compelling explanation for the observed trend of photocurrent enhancements in NM/F heterojunctions relative to their NH_2-MIL-125 counterparts.

To substantiate the proposed S-scheme charge transfer mechanism, both *ex situ* and *in situ* irradiated XPS (Fig. S29) measurements were implemented on the NM/F samples, with their individual components serving as reference samples. In the *ex situ* spectra, Ti 2p peaks of NM(S)/F, NM(T)/F, and NM(O)/F shift to higher binding energies by 0.06, 0.10, and 0.14 eV, respectively, compared with their corresponding NM(S), NM(T), and NM(O) counterparts (Fig. 4e and S30). Conversely, relative to bare Fe_2O_3, Fe 2p peaks of NM(S)/F, NM(T)/F, and NM(O)/F move to lower binding energies by 0.19, 0.31, and 0.51 eV, respectively. These shifts provide solid evidence for the diffusion of free electrons from NH_2-MIL-125 to Fe_2O_3, resulting in the formation of IEFs and bending of energy bands.[40] The peak shifts of NM/F become more prominent as the {111}/{001} facet ratio of NH_2-MIL-125 increases, substantiating that a more significant redistribution of free electrons leads to augmented IEF and BB.[22,25] Furthermore, upon visible light irradiation, the Ti 2p peaks of NM(S)/F, NM(T)/F, and NM(O)/F exhibit negative shifts in binding energies by 0.10, 0.12, and 0.23 eV, respectively, whilst the Fe 2p peaks present positive shifts in binding energies by 0.20, 0.29, and 0.48 eV, respectively, consolidating a progressively enhanced S-scheme transfer of photoelectrons from Fe_2O_3 to NH_2-MIL-125 with the increasing proportion of NH_2-MIL-125{111} facets.[41] When compared to their individual NH_2-MIL-125 and Fe_2O_3 components or under light irradiation, NM/F@T samples demonstrate the same facet-dependent deviation trend in both Ti and Fe peaks as observed in the NM/F samples (Fig. S31). These findings unveil that T-COF introduction does not significantly alter the directions and relative intensities of the IEF between Fe_2O_3 and different NH_2-MIL-125, nor does it substantially modify the resulting orientations and relative efficiencies of photoelectron movement from the former to the latter. Nevertheless, the deviation degrees for Ti and Fe peaks under light irradiation are less pronounced and more significant, respectively, compared to their corresponding NM/F counterparts. This trend clearly indicates that the T-COF coating weakens the carrier separation in NH_2-MIL-125 while enhancing it in Fe_2O_3. To further elucidate the function of T-COF in steering the charge kinetics, the N 1s spectra of NM/F@T samples were deconvoluted into three peaks, corresponding to –N=$^+$ and –NH–$^+$ peaks of NH_2-MIL-125 and the –C=N–C– peak of T-COF, respectively (Fig. S31).[42,43] Compared to pristine T-COF, the –C=N–C– peak of NM/F@T samples exhibits a notable shift towards higher binding energies, suggesting that T-COF acts as a free electron donor upon hybridization with NM/F. Moreover, the peak shifts for NM(S)/F@T, NM(T)/F@T, and NM(O)/F@T are 0.23, 0.14, and 0.12 eV, respectively, signifying that T-COF becomes less electron-deficient as the proportion of NH_2-MIL-125{111} facets increases (Fig. 4f and S31). When irradiated by visible light, the –C=N–C– peak of NM(S)/F@T, NM(T)/F@T, and NM(O)/F@T undergoes negative shifts of 0.27, 0.15, and 0.12 eV, respectively. This observation demonstrates that T-COF serves as a photoelectron acceptor, with its electron-accepting capability progressively decreasing as the proportion of NH_2-MIL-125{111} facets grows.

Based on preceding analyses, a dual S-scheme charge transfer model is proposed for the NM/F@T samples. As illustrated in Fig. 4d, when T-COF and NM/F come into contact, T-COF naturally donates free electrons to NM/F to align their E_F. This generates an extra IEF pointed from T-COF to Fe_2O_3, inducing an upward BB of T-COF and a downward BB of Fe_2O_3 around their interface. Upon exposure to light irradiation, the generated IEFs and BBs drive the transfer of Fe_2O_3 electrons and their recombination with holes in NH_2-MIL-125 and T-COF. Simultaneously, photoelectrons in NH_2-MIL-125 and T-COF, along with holes in Fe_2O_3—all possessing strong redox capabilities—are spatially separated, enabling efficient redox reactions. The additional IEF and BB between T-COF and Fe_2O_3 expedite the S-scheme transfer and recombination of pointless charges, thus giving rise to a more thorough separation of powerful carriers in NM/F@T samples compared to their NM/F counterparts. Due to competitive recombination between Fe_2O_3 electrons with holes from NH_2-MIL-125 and T-COF, the charge separation efficiency in NH_2-MIL-125 is attenuated upon T-COF introduction, thereby diminishing the number of active

electrons in NH_2-MIL-125 available for reduction reactions. Furthermore, as the E_F of NM(S), NM(T), and NM(O) progressively shifts to higher positions, their respective combinations with Fe_2O_3 result in a gradual elevation of the aligned E_F for NM(S)/F, NM(T)/F, and NM(O)/F. Correspondingly, the E_F difference between NM/F and T-COF decreases as the fraction of NH_2-MIL-125{111} facets increases. This debilitates free electron redistribution, consequently weakening both the IEF and BB, and mitigating the S-scheme charge transfer between Fe_2O_3 and T-COF. The gradual weakening of the IEF is further substantiated by the progressively decreasing Zeta potentials of NM(S)/F@T, NM(T)/F@T, and NM(O)/F@T from 14.6 mV to 9.3 mV, and ultimately to 6.8 mV (Fig. S32).[44] As a result, charge separation enhancements observed in NM(S)/F@T, NM(T)/F@T, and NM(O)/F@T relative to their corresponding NM/F counterparts gradually decline, which aligns with the observed PEC results. Clearly, as the NH_2-MIL-125{111} facets become more exposed, the IEF strength and the resulting S-scheme charge transfer efficiency between NH_2-MIL-125 and Fe_2O_3, as well as between Fe_2O_3 and T-COF, demonstrate inverse trends, leading to the separation of more active electrons on the NH_2-MIL-125 side and less on the T-COF side (Fig. 4d).

Facet-dependent catalytic dynamics of NM/F and NM/F@T

Beyond charge kinetics, the influence of Fe_2O_3 and T-COF on the surface reactivities of NM/F and NM/F@T was also deliberated. Initially, we calculated the CO_2 and H_2O adsorption energies on NH_2-MIL-125{001}, NH_2-MIL-125{111}, Fe_2O_3{012}, and T-COF surfaces (Fig. S33). As displayed in Fig. 5a, the CO_2 adsorption energy for T-COF (−1.18 eV) is more negative compared to those of NH_2-MIL-125 (−0.62 and −0.91 eV) and Fe_2O_3 (−0.51 eV), suggesting that CO_2 molecule adsorption is thermodynamically most favorable on the outer T-COF shell. CO_2 adsorption isotherms in Fig. S34 confirm this finding: while implanting Fe_2O_3 on NM(S) reduces the CO_2 adsorption capacity of NM(S)/F, subsequent wrapping with T-COF significantly enhances the CO_2 uptake of NM(S)/F@T. Moreover, H_2O adsorption energies on NH_2-MIL-125{001} (−0.71 eV) and NH_2-MIL-125{111} (−0.65 eV) are more negative than those of Fe_2O_3 (−0.36 eV) and T-COF (−0.49 eV), certifying that the NH_2-MIL-125 core possesses a substantially higher affinity for H_2O molecule adsorption. Subsequently, LSV curves were obtained in Ar- and CO_2-saturated electrolytes to gain insight into CO_2 and H_2O activation behaviors. For both NM(S) and NM(S)/F, the overpotentials under an Ar atmosphere are significantly smaller than those under a CO_2 atmosphere, implying that H_2 evolution is the predominant reaction on the catalyst surface, consistent with the photocatalytic results (Fig. S35).[45] Unlike NM(S) and NM(S)/F, the LSV overpotential of NM(S)/F@T in the Ar-saturated electrolyte is significantly larger than that in the CO_2-saturated electrolyte, suggesting that the newly introduced T-COF has a greater tendency to reduce CO_2 molecules rather than protons.[46] Using DMPO as a spin-trapping agent to probe the generation of hydrogen radicals during the reaction process, both NM(S) and NM(S)/F display nine strong peaks with an intensity ratio of approximately 1 : 1 : 2 : 1 : 2 : 1 : 2 : 1 : 1 in an Ar atmosphere, corresponding to DMPO-H adducts (Fig. S36).[47] Contrarily, the peaks for bare Fe_2O_3 are extremely weak. This suggests that NH_2-MIL-125 is primarily responsible for the generation of active hydrogen. Fig. 5b shows the Gibbs free

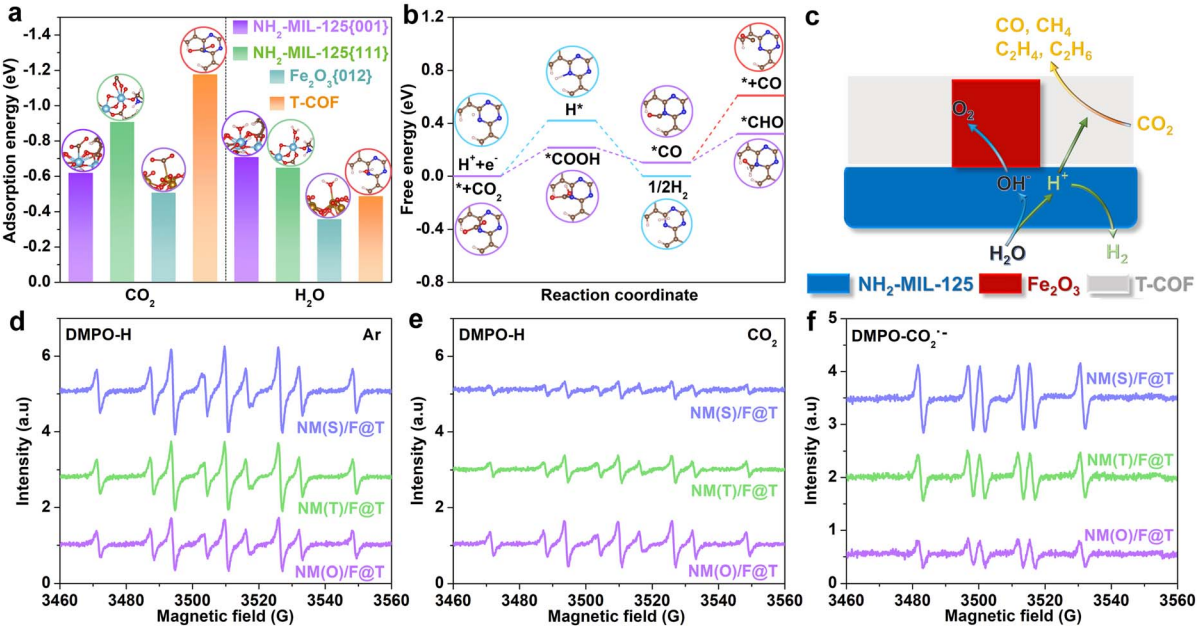

Fig. 5 Facet-dependent surface reactivities of NM/F@T: (a) comparative adsorption energies of CO_2 and H_2O on NH_2-MIL-125{001}, NH_2-MIL-125{111}, Fe_2O_3{012}, and T-COF surfaces; (b) Gibbs free energy diagrams for H_2 evolution and CO_2 reduction over T-COF; (c) schematic illustrating the surface reaction mechanisms in NM/F and NM/F@T; (d and e) EPR spectra of DMPO-H over NM/F@T samples under (d) Ar and (e) CO_2 atmospheres; (f) EPR spectra of DMPO–$CO_2^{\bullet-}$ over NM/F@T samples.

energies for CO_2 reduction and H_2 evolution on the T-COF surface. The free energy of H adsorption is calculated to be 0.42 eV, while converting CO_2 to *CO requires overcoming a *COOH formation energy of 0.22 eV, indicating that the initial steps of CO_2 reduction are more thermodynamically favorable than H_2 evolution. Moreover, the hydrogenation of *CO to *CHO entails a lower energy barrier compared to the desorption of *CO. This demonstrates that CO_2 hydrogenation to form CH_4 is more energetically favorable than CO_2 deoxygenation to produce CO. Furthermore, LSV measurements were conducted to evaluate the O_2 evolution reaction (OER) kinetics of NM(S), NM(S)/F, and NM(S)/F@T. As depicted in Fig. S37, the onset potential of NM(S)/F is substantially lower than that of NM(S) but similar to that of NM(S)/F@T, confirming that Fe_2O_3 plays a crucial role in catalyzing the OER. Ultimately, based on the experimental and theoretical results, Fig. 5c illustrates the operating principle of the NM/F and NM/F@T systems for photocatalytic CO_2 reduction coupled with H_2O oxidation. NH_2-MIL-125 samples primarily catalyze the H_2O dissociation into H^+ and OH^- species, and subsequently reduce H^+ to H_2. The introduction of Fe_2O_3 significantly enhances charge separation, enabling a higher population of active electrons to participate in H_2 evolution on the NH_2-MIL-125 surface while simultaneously facilitating OH^- oxidation to O_2 on the Fe_2O_3 surface, which accounts for the improved H_2 and O_2 evolution observed in the NM/F samples. Upon T-COF coating, the number of NH_2-MIL-125 electrons engaging in the reduction of H^+ decreases. Consequently, unconsumed reactive hydrogen species diffuse from the NH_2-MIL-125 core to the T-COF shell, where they participate in CO_2 upcycling. This process suppresses H_2 evolution on the NH_2-MIL-125 surface and promotes CO_2 hydrogenation within the T-COF shell, effectively elucidating the enhanced activity and selectivity for CO, CH_4, C_2H_4, and C_2H_6 production in the NM/F@T samples compared to their NM/F counterparts.

To further clarify the impact of NH_2-MIL-125 exposed facets on the surface reactivities of NM/F@T samples, we conducted a comparative analysis of DMPO-H signals under light irradiation. In an Ar atmosphere, all NM/F@T samples generate DMPO-H signals, with signal intensities gradually decreasing as the percentage of NH_2-MIL-125{111} facets increases (Fig. 5d). This trend indicates a declining formation of active hydrogen, consistent with the facet-dependent H_2O splitting behavior of NH_2-MIL-125. Upon replacing Ar with CO_2, the DMPO-H signals exhibit distinct responses: NM(S)/F@T shows a dramatic weakening, NM(T)/F@T demonstrates a moderate reduction, and NM(O)/F@T displays a slight attenuation (Fig. 5e). These observations suggest that active hydrogen is consumed during the CO_2 photoreduction process, with the consumption rate decreasing progressively as the proportion of NH_2-MIL-125{111} facets rises.[48] This results express that more H^+ diffuses from NH_2-MIL-125{001} facets to the T-COF shell for participating in CO_2 photoreduction compared to NH_2-MIL-125{111} facets. During EPR measurements conducted in a CO_2 atmosphere, we also observed DMPO–$CO_2^{\bullet-}$ signals when transitioning the catalyst solvent from water to ACN/triethanolamine aqueous solution, suggesting CO_2 activation *via* the electron reduction route: $CO_2 + e^- \rightarrow CO_2^{\bullet-}$ (Fig. 5f).[49] When exposed to equivalent irradiation periods, NM(S)/F@T exhibits the highest DMPO–$CO_2^{\bullet-}$ signal intensity, followed by NM(T)/F@T, and then NM(O)/F@T. This observation indicates that greater exposure of NH_2-MIL-125{001} facets enhances the activation of CO_2 molecules on the T-COF surface.

Following CO_2 activation, intermediates were generated during their conversion to final products. These intermediates were dynamically monitored using *in situ* diffuse reflectance infrared Fourier transform spectra (DRIFTS) under a humid CO_2 atmosphere. To investigate the influence of NH_2-MIL-125 facets on the CO_2 photoreduction pathway, DRIFTS measurements were performed on NM(S)/F@T and NM(O)/F@T under identical conditions (Fig. 6a and b). Prior to light irradiation, only peaks of adsorbed CO_2 were observed for both samples, including asymmetric stretching of CO_2 at approximately 2365–2570 cm^{-1} and overtone bands of CO_2 at around 3575–3875 cm^{-1}.[50,51] Upon photoirradiation, multiple peaks associated with CO_2 reduction intermediates emerge, with their signal intensities gradually increasing as irradiation continues, such as HCO_3^- (*ca.* 1169–1257, 1378, 1409 cm^{-1}), b-CO_3^{2-} (*ca.* 1328, 1353, and 1600 cm^{-1}), m-CO_3^{2-} (*ca.* 1430, 1466, and 1522 cm^{-1}), $\cdot CO_2^-$ (*ca.* 1686 cm^{-1}), and c-CO_3^{2-} (*ca.* 1713–1781 cm^{-1}).[51–54] Additionally, *COOH and *CO species were detected at around 1557 and 2043 cm^{-1}, respectively.[49,55] Both are crucial intermediates in the formation of CO and hydrocarbons. Besides, a peak at approximately 2100 cm^{-1} indicates the formation of CO, aligning well with the proposed reaction pathway in the Gibbs free energy calculations: $CO_2 \rightarrow$ *COOH $\rightarrow$ *CO $\rightarrow$ CO.[56] Notably, compared to NM(O)/F@T, NM(S)/F@T exhibits substantially higher intensities of $\cdot CO_2^-$ and *COOH, further supporting its superior ability to activate and protonate CO_2. Moreover, the *CO and CO peak intensities of NM(S)/F@T are lower than those of NM(O)/F@T, consistent with the former's faster *CO consumption rate and inferior CO productivity and selectivity relative to the latter. Furthermore, with extended illumination time, NM(S)/F@T displays a more pronounced increase in CO_2 peak intensity compared to NM(O)/F@T. This enhancement can be attributed to the more rapid increase in electron density on the T-COF surface of NM(S)/F@T, which provides more favorable conditions for the adsorption of Lewis acidic CO_2 molecules.

Additional characteristic intermediates involved in CH_4 formation were also recorded in the DRIFTS of NM(S)/F@T and NM(O)/F@T, including *CHO (*ca.* 1083 cm^{-1}), *CH_3O (*ca.* 1046, 1129, and 2847 cm^{-1}), *CH_2 (*ca.* 2918 cm^{-1}), and *CH_3 (*ca.* 2947 cm^{-1}) (Fig. 6a and b).[57,58] These intermediates indicate a deeper hydrogenation and deoxygenation pathway: *CO $\rightarrow$ *CHO $\rightarrow$ *CH_2O $\rightarrow$ *CH_3O $\rightarrow$ *CH_2 $\rightarrow$ *CH_3 $\rightarrow$ CH_4. During the identical irradiation duration, NM(S)/F@T experiences a more pronounced increase in signal intensities of these intermediates relative to NM(O)/F@T. This outcome certifies the superior activity of NM(S)/F@T in CO_2 methanation. Another notable distinction between the two samples lies in the peaks of *OCCO (1519 cm^{-1}), *OCCOH (1565 cm^{-1}), and *C_2H_4 (1442 cm^{-1}), which are observable in the DRIFTS of NM(O)/F@T but absent in that of NM(S)/F@T.[59,60] This observation suggests

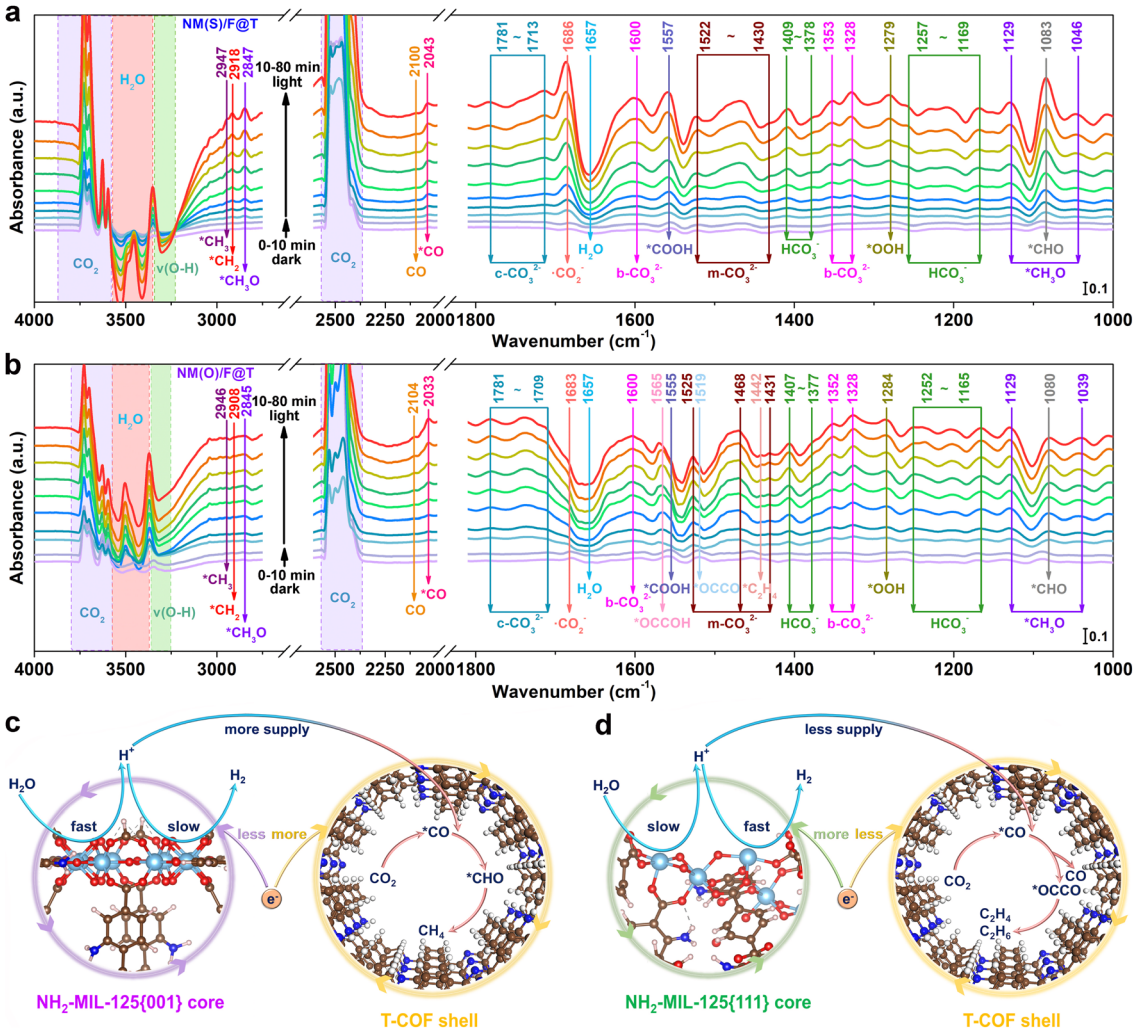

Fig. 6 Facet-dependent photocatalytic mechanisms of NM/F@T: (a and b) *in situ* DRIFTS of photocatalytic CO_2 reduction over (a) NM(S)/F@T and (b) NM(O)/F@T; (c and d) schematic illustration of the photocatalytic mechanisms of NM/F@T when NH_2-MIL-125 is exposed with (c) {001} and (d) {111} facets.

that NM(O)/F@T is more conducive to the C–C coupling of *CO to form *OCCO, as well as the subsequent hydrogenation of the *OCCO intermediate to generate C_2H_4 and C_2H_6, consistent with the photocatalytic results. Aside from carbon-containing species, NM(S)/F@T and NM(O)/F@T also show distinctive H_2O peaks in their DRIFTS: one depletion peak centered at 1657 cm^{-1} corresponds to the bending vibration of H_2O, two negative peaks ranging from 3351 to 3572 cm^{-1} represent the stretching vibrations of adsorbed H_2O, and one negative peak at around 3310 cm^{-1} is attributed to the stretching vibrations of surface-bonded O–H.[61–65] For NM(S)/F@T, the intensity variation of these peaks is more pronounced when compared with NM(O)/F@T, indicating more rapid consumption of both physisorbed and chemisorbed H_2O molecules. Furthermore, one positive peak at around 1279 cm^{-1} is identified as the OOH* species, suggesting the conversion of H_2O to O_2 through the pathway: $H_2O \rightarrow *OH \rightarrow *O \rightarrow *OOH \rightarrow O_2$.[66]

On the basis of the above discussion, we provided a comprehensive visualization of the facet-dependent photocatalytic reaction mechanisms in NM/F and NM/F@T. As depicted in Fig. 6c, the NH_2-MIL-125{001} facets demonstrate superior H_2O activation capabilities, splitting more H_2O molecules into H^+ and OH^- species. However, the relatively inefficient charge separation between NH_2-MIL-125{001} and Fe_2O_3 constrains the photoelectron participation in H^+ reduction on the NH_2-MIL-125{001} surface, consequently moderating the H_2 production enhancement in NM/F. Upon T-COF coating, the higher charge separation efficiency between Fe_2O_3 and T-COF results in an asymmetric distribution of active electrons between NH_2-MIL-125 and T-COF, reducing the electron feeding to the NH_2-MIL-125 core for H_2 generation. As a result, a larger number of unconsumed H^+ migrate to the T-COF shell. This facilitates the rapid protonation of *CO intermediates to *CHO, preventing their desorption from the catalyst surface as CO and instead fostering their hydrogenation to CH_4. Additionally, an increased quantity of active electrons in the T-COF shell engages in the conversion of CO_2 molecules, also promoting the 8-electron reduction of CO_2 to CH_4. In

comparison, as illustrated in Fig. 6d, the NH_2-MIL-125{111} facets demonstrate inferior H_2O activation abilities, reducing the number of H^+ generated through H_2O dissociation. Nevertheless, due to the higher charge separation efficiency between NH_2-MIL-125{111} and Fe_2O_3, more electrons participate in H^+ reduction, boosting H_2 production in NM/F. This decreases the amount of H^+ diffusion to T-COF for CO_2 reduction, making *CO more prone to desorption than hydrogenation. Besides, the relatively lower charge separation efficiency between Fe_2O_3 and T-COF reduces the number of T-COF photoelectrons partaking in the activation and conversion of CO_2. As such, the 2-electron reduction of CO_2 to CO becomes more favorable compared to CO_2 methanation. Furthermore, the sluggish *CO hydrogenation process increases *CO coverage on the T-COF sites, facilitating *CO–*CO coupling to form *OCCO and promoting the generation of C_2 products. Notably, while reducing CO_2 to C_2H_4 and C_2H_6 requires 12 and 14 electrons and protons, respectively, on average, each CO_2 molecule needs only 6 and 7 electrons and protons—fewer than the 8 electrons and protons required to produce CH_4. Therefore, the formation of C_2 products is not hindered by the limited availability of electrons and protons. Overall, the different distributions of active electrons and protons on NH_2-MIL-125 and T-COF, enabled by the S-scheme and dual S-scheme heterojunctions, should be the origin of the facet-dependent photocatalytic performance of NM/F and NM/F@T.

Conclusions

To conclude, we developed dual S-scheme heterojunctions consisting of H_2O dissociation, CO_2 reduction, and O_2 evolution catalysts for photocatalytic reduction of CO_2 with H_2O and modulated the product selectivities by regulating the exposed facets of supports in the ternary heterojunctions. In the designed three-in-one photosynthetic systems, NH_2-MIL-125 cores activate H–OH dissociation, after which the generated H^+ and OH^- species migrate to T-COF shells and Fe_2O_3 inserts for CO_2 reduction and O_2 evolution, respectively. Combining experimental characterization studies and theoretical calculations demonstrates that the H_2O dissociation abilities and S-scheme charge transfer efficiencies in the fabricated NM/F@T heterojunctions strongly depend on the exposed facets of NH_2-MIL-125 supports. A higher percentage of {001} facet exposure accelerates H_2O splitting, producing more H^+ while also creating an uneven distribution of active electrons—fewer on the NH_2-MIL-125 side and more on the T-COF side. Consequently, H_2 evolution on the NH_2-MIL-125 core is effectively suppressed, allowing more H^+ to engage in CO_2 hydrogenation on the T-COF shell. This enhances the tendency of *CO intermediates to undergo protonation rather than desorption or C–C coupling. The result is a gradual increase in CH_4 production accompanied by a decline in H_2, CO, C_2H_4, and C_2H_6 generation, with champion CH_4 activity and selectivity achieved by NM(S)/F@T with the highest {001} facet exposure. This work establishes a groundbreaking approach for fostering the performance of heterostructured photocatalysts in PCET reactions through targeted facet engineering that precisely modulates electron and proton dynamics.

Author contributions

Hulin Shi: conceptualization, investigation, methodology, writing – original draft. Zengrong Li: methodology, software, formal analysis, validation. Shenglan Chen: methodology, software. Yangtao Yao: investigation, validation. Linyi Wu: data curation. Ruowen Shao: investigation. Chang Sheng: investigation. Shuxian Zhong: validation, resources, supervision. Dongmei Wang: validation, resources. Yuling Zhao: validation, resources. Leihong Zhao: validation, resources. Song Bai: conceptualization, formal analysis, supervision, writing – review & editing, funding acquisition, project administration.

Conflicts of interest

There are no conflicts to declare.

Data availability

Experimental details, computational details, tables, additional figures and references are available in the SI.

The data supporting this article have been included as part of the SI. Supplementary information is available. See DOI: **https://doi.org/10.1039/d5sc03122b**.

Acknowledgements

This work was supported by the National Natural Science Foundation of China (No. 21603191 and 22572174), Zhejiang Provincial Natural Science Foundation of China (No. LMS25B030006 and LY20B030003), Key Research and Development Program of Zhejiang Province (No. 2023C03148), and Foundation of Science and Technology Bureau of Jinhua (No. 2024-4-011). The authors would like to thank ShiyanjiaLab (**https://www.shiyanjia.com**) for contact angle measurements.

Notes and references

1 S. Yoshino, T. Takayama, Y. Yamaguchi, A. Iwase and A. Kudo, *Acc. Chem. Res.*, 2022, **55**, 966–977.
2 T. Kong, Y. Jiang and Y. Xiong, *Chem. Soc. Rev.*, 2020, **49**, 6579–6591.
3 E. Gong, S. Ali, C. B. Hiragond, H. S. Kim, N. S. Powar, D. Kim, H. Kim and S. In, *Energy Environ. Sci.*, 2022, **15**, 880–937.
4 U. Ulmer, T. Dingle, P. N. Duchesne, R. H. Morris, A. Tavasoli, T. Wood and G. A. Ozin, *Nat. Commun.*, 2019, **10**, 3169.
5 S. Cheng, Z. Sun, K. H. Lim, T. Z. H. Gani, T. Zhang, Y. Wang, H. Yin, K. Liu, H. Guo, T. Du, L. Liu, G. Li, Z. Yin and S. Kawi, *Adv. Energy Mater.*, 2022, **12**, 2200389.
6 W. Tu, Y. Zhou and Z. Zou, *Adv. Mater.*, 2014, **26**, 4607–4626.
7 C. Chen, M. Wu, Y. Xu, C. Ma, M. Song and G. Jiang, *J. Am. Chem. Soc.*, 2024, **146**, 9163–9171.

8 X. Cui, H. Bai, J. Zhang, R. Liu, H. Yu, Y. Wang, T. Kong, M. Gao, Z. Lu and Y. Xiong, *Nat. Commun.*, 2024, **15**, 9048.
9 D. Cong, J. Sun, Y. Pan, X. Fang, L. Yang, W. Zhou, T. Yu, Z. Li, C. Liu and W. Deng, *Angew. Chem., Int. Ed.*, 2024, **63**, e202316991.
10 W. Zheng, X. Yang, Z. Li, B. Yang, Q. Zhang, L. Lei and Y. Hou, *Angew. Chem., Int. Ed.*, 2023, **62**, e202307283.
11 W. Ma, S. Xie, T. Liu, Q. Fan, J. Ye, F. Sun, Z. Jiang, Q. Zhang, J. Cheng and Y. Wang, *Nat. Catal.*, 2020, **3**, 478–487.
12 Y. Xu, W. Li, H. Fu, X. Zhang, J. Zhao, X. Wu, H. Yuan, M. Zhu, S. Dai, P. Liu and H. Yang, *Angew. Chem., Int. Ed.*, 2023, **62**, e202217296.
13 J. Fu, K. Jiang, X. Qiu, J. Yu and M. Liu, *Mater. Today*, 2020, **32**, 222–243.
14 W. Wang, W. Zhang, C. Deng, H. Sheng and J. Zhao, *Angew. Chem., Int. Ed.*, 2024, **63**, e202317969.
15 S. Chen, Y. Qi, C. Li, K. Domen and F. Zhang, *Joule*, 2018, **2**, 2260–2288.
16 L. Zhang, J. Zhang, H. Yu and J. Yu, *Adv. Mater.*, 2022, **34**, 2107668.
17 L. Wang, B. Zhu, J. Zhang, J. B. Ghasemi, M. Mousavi and J. Yu, *Matter*, 2022, **5**, 4187–4211.
18 F. Cao, X. Zhang, X. Niu, X. Lin, T. Wu, S. Zhong, H. Lin, L. Zhao and S. Bai, *ACS Catal.*, 2024, **14**, 12529–12540.
19 T. F. Qahtan, T. O. Owolabi, O. E. Olubi and A. Hazam, *Coord. Chem. Rev.*, 2024, **514**, 215839.
20 R. Guo, J. Wang, Z. Bi, X. Chen, X. Hu and W. Pan, *Small*, 2023, **19**, 2206314.
21 S. Das, J. Pérez-Ramírez, J. Gong, N. Dewangan, K. Hidajat, B. C. Gates and S. Kawi, *Chem. Soc. Rev.*, 2020, **49**, 2937–3004.
22 Y. Zhang, F. Cao, S. Zhao, J. Zhang, S. Zhong, H. Mao, L. Zhao and S. Bai, *Adv. Funct. Mater.*, 2025, **35**, 2413830.
23 S. Bai, L. Wang, Z. Li and Y. Xiong, *Adv. Sci.*, 2017, **4**, 1600216.
24 W. Tu, W. Guo, J. Hu, H. He, H. Li, Z. Li, W. Luo, Y. Zhou and Z. Zou, *Mater. Today*, 2020, **33**, 75–86.
25 Y. Xi, W. Chen, W. Dong, Z. Fan, K. Wang, Y. Shen, G. Tu, S. Zhong and S. Bai, *ACS Appl. Mater. Interfaces*, 2021, **13**, 39491–39500.
26 S. Wang, G. Liu and L. Wang, *Chem. Rev.*, 2019, **119**, 5192–5247.
27 S. Hu, M. Liu, X. Guo, Z. Kuang, K. Li, C. Song and G. Zhang, *J. Solid State Chem.*, 2018, **262**, 237–243.
28 R. Wang, C. Xu, J. Sun and L. Gao, *Sci. Rep.*, 2014, **4**, 7171.
29 Y. Wang, Z. Hu, W. Wang, H. He, L. Deng, Y. Zhang, J. Huang, N. Zhao, G. Yu and Y. Liu, *Chem. Sci.*, 2021, **12**, 16065–16073.
30 J. Dong, Y. Wang, G. Liu, Y. Cheng and D. Zhao, *CrystEngComm*, 2017, **19**, 4899–4904.
31 L. Liu, S. Du, Y. Xiao, X. Guo, S. Jin, G. Shao and F. Zhang, *Appl. Catal., B*, 2023, **338**, 123094.
32 X. Cheng, X. Dao, S. Wang, J. Zhao and W. Sun, *ACS Catal.*, 2021, **11**, 650–658.
33 S. Wang, B. Jiang, J. Henzie, F. Xu, C. Liu, X. Meng, S. Zou, H. Song, Y. Pan, H. Li, J. Yu, H. Chen and J. Ye, *Nat. Commun.*, 2023, **14**, 2534.
34 Z. Xin, Y. Gao, Y. Gao, H. Song, J. Zhao, F. Fan, A. Xia, X. Li, C. Tung and L. Wu, *Adv. Mater.*, 2022, **34**, 2106662.
35 J. Ding, M. Chen, X. Du, R. Shang, M. Xia, J. Hu and Q. Zhong, *Catal. Lett.*, 2019, **149**, 3287–3295.
36 D. Sun, L. Ye and Z. Li, *Appl. Catal., B*, 2015, **164**, 428–432.
37 C. Chen, L. Chen, Y. Hu, K. Yan, T. Wang, Y. Huang, C. Gao, J. Mao, S. Liu and B. Li, *J. Energy Chem.*, 2023, **86**, 599–608.
38 X. Chu, S. Liu, B. Luan, Y. Zhang, Y. Xi, L. Shao, F. Zhang and Y. Lan, *Angew. Chem., Int. Ed.*, 2025, **64**, e202422940.
39 L. Hu, Y. Zhang, Q. Lin, F. Cao, W. Mo, S. Zhong, H. Lin, L. Xie, L. Zhao and S. Bai, *Chin. J. Catal.*, 2025, **68**, 311–325.
40 Z. Li, P. Wang, C. Ren, L. Wu, Y. Yao, S. Zhong, H. Lin, L. Zhao, Y. Gao and S. Bai, *ACS Catal.*, 2025, **15**, 828–840.
41 L. Wang, B. Cheng, L. Zhang and J. Yu, *Small*, 2021, **17**, 2103447.
42 B. Zhang, J. Zhang, X. Tan, D. Shao, J. Shi, L. Zheng, J. Zhang, G. Yang and B. Han, *ACS Appl. Mater. Interfaces*, 2018, **10**, 16418–16423.
43 F. Rastegari, S. Asghari, I. Mohammadpoor-Baltork, H. Sabzyan, S. Tangestaninejad, M. Moghadam and V. Mirkhani, *J. Hazard. Mater.*, 2024, **476**, 135075.
44 J. Hu, B. Li, X. Li, T. Yang, X. Yang, J. Qu, Y. Cai, H. Yang and Z. Lin, *Adv. Mater.*, 2024, **36**, 2412070.
45 P. Li, G. Luo, S. Zhu, L. Guo, P. Qu and T. He, *Appl. Catal., B*, 2020, **274**, 119115.
46 F. Wang, T. Hou, X. Zhao, W. Yao, R. Fang, K. Shen and Y. Li, *Adv. Mater.*, 2021, **33**, 2102690.
47 Z. Chang, G. Meng, Y. Chen, C. Chen, S. Han, P. Wu, L. Zhu, H. Tian, F. Kong, M. Wang, X. Cui and J. Shi, *Adv. Mater.*, 2023, **35**, 2304508.
48 T. Bao, Y. Xi, C. Zhang, P. Du, Y. Xiang, J. Li, L. Yuan, C. Yu and C. Liu, *Natl. Sci. Rev.*, 2024, **11**, nwae093.
49 M. Zhou, Z. Wang, A. Mei, Z. Yang, W. Chen, S. Ou, S. Wang, K. Chen, P. Reiss, K. Qi, J. Ma and Y. Liu, *Nat. Commun.*, 2023, **14**, 2473.
50 X. Yang, S. Wang, N. Yang, W. Zhou, P. Wang, K. Jiang, S. Li, H. Song, X. Ding, H. Chen and J. Ye, *Appl. Catal., B*, 2019, **259**, 118088.
51 W. He, Y. Wei, J. Xiong, Z. Tang, W. Song, J. Liu and Z. Zhao, *Chem. Eng. J.*, 2022, **433**, 133540.
52 J. Sheng, Y. He, J. Li, C. Yuan, H. Huang, S. Wang, Y. Sun, Z. Wang and F. Dong, *ACS Nano*, 2020, **14**, 13103–13114.
53 R. Wang, Z. Wang, S. Wan, Q. Liu, J. Ding and Q. Zhong, *Chem. Eng. J.*, 2022, **434**, 134434.
54 J. Tian, Y. Zhang, Z. Shi, Z. Liu, Z. Zhao, J. Li, N. Li and H. Huang, *Angew. Chem., Int. Ed.*, 2025, **64**, e202418496.
55 X. Zu, Y. Zhao, X. Li, R. Chen, W. Shao, Z. Wang, J. Hu, J. Zhu, Y. Pan, Y. Sun and Y. Xie, *Angew. Chem., Int. Ed.*, 2021, **60**, 13840–13846.
56 Y. Ma, Y. Zhang, G. Xie, Z. Huang, L. Peng, C. Yu, X. Xie, S. Qu and N. Zhang, *ACS Catal.*, 2024, **14**, 1468–1479.
57 X. Li, Y. Sun, J. Xu, Y. Shao, J. Wu, X. Xu, Y. Pan, H. Ju, J. Zhu and Y. Xie, *Nat. Energy*, 2019, **4**, 690–699.
58 S. Barman, A. Singh, F. A. Rahimi and T. K. Maji, *J. Am. Chem. Soc.*, 2021, **143**, 16284–16292.

59 Z. Xie, L. Li, S. Gong, S. Xu, H. Luo, D. Li, H. Chen, M. Chen, K. Liu, W. Shi, D. Xu and Y. Lei, *Angew. Chem., Int. Ed.*, 2024, **63**, e202410250.
60 Z. Xie, S. Xu, L. Li, S. Gong, X. Wu, D. Xu, B. Mao, T. Zhou, M. Chen, X. Wang, W. Shi and S. Song, *Nat. Commun.*, 2024, **15**, 2422.
61 C. Mao, J. Wang, Y. Zou, Y. Shi, C. J. Viasus, J. Y. Y. Loh, M. Xia, S. Ji, M. Li, H. Shang, M. Ghoussoub, Y. Xu, J. Ye, Z. Li, N. P. Kherani, L. Zheng, Y. Liu, L. Zhang and G. A. Ozin, *J. Am. Chem. Soc.*, 2023, **145**, 13134–13146.
62 J. Xu, H. Jin, T. Lu, J. Li, Y. Liu, K. Davey, Y. Zheng and S. Qiao, *Sci. Adv.*, 2023, **9**, eadh1718.
63 S. Si, H. Shou, Y. Mao, X. Bao, G. Zhai, K. Song, Z. Wang, P. Wang, Y. Liu, Z. Zheng, Y. Dai, L. Song, B. Huang and H. Cheng, *Angew. Chem., Int. Ed.*, 2022, **61**, e202209446.
64 H. Shi, R. Shao, S. Lei, M. Zhou, X. Yuan, Z. Chen, S. Wei, S. Zhong, Y. Zhao, L. Zhao and S. Bai, *Appl. Catal. B Environ. Energy*, 2025, **373**, 125363.
65 S. Zhang, Y. Ma, C. Yu, Z. Huang, R. Zhan, Y. Wang, X. Xie and N. Zhang, *Chem. Sci.*, 2025, **16**, 5241–5251.
66 B. Su, Y. Kong, S. Wang, S. Zuo, W. Lin, Y. Fang, Y. Hou, G. Zhang, H. Zhang and X. Wang, *J. Am. Chem. Soc.*, 2023, **145**, 27415–27423.